

Predictive approach of heat transfer for the modelling of large-scale latent heat storages

Clément Beust, Erwin Franquet, Jean-Pierre Bedecarrats, Pierre Garcia

▶ **To cite this version:**

Clément Beust, Erwin Franquet, Jean-Pierre Bedecarrats, Pierre Garcia. Predictive approach of heat transfer for the modelling of large-scale latent heat storages. Renewable Energy, 2020, 10.1016/j.renene.2020.04.135 . hal-02566401

HAL Id: hal-02566401

https://univ-pau.hal.science/hal-02566401

Submitted on 3 Jun 2022

HAL is a multi-disciplinary open access archive for the deposit and dissemination of scientific research documents, whether they are published or not. The documents may come from teaching and research institutions in France or abroad, or from public or private research centers.

L'archive ouverte pluridisciplinaire **HAL**, est destinée au dépôt et à la diffusion de documents scientifiques de niveau recherche, publiés ou non, émanant des établissements d'enseignement et de recherche français ou étrangers, des laboratoires publics ou privés.



Distributed under a Creative Commons Attribution - NonCommercial 4.0 International License

Version of Record: https://www.sciencedirect.com/science/article/pii/S096014812030673X
Manuscript_a05ac730b55b7fe3232f49f7da4c39de

Predictive approach of heat transfer for the modeling of large-scale latent heat storages

Clément Beust[a,b], Erwin Franquet[b,*], Jean-Pierre Bédécarrats[b], Pierre Garcia[a]

[a] Univ. Grenoble Alpes, CEA, LITEN, DTBH, Laboratoire de Stockage Thermique, 17 avenue des Martyrs, 38054 Grenoble Cedex 9

[b] Universite de Pau et des Pays de l'Adour, E2S UPPA, LaTEP, Pau, France
Laboratoire de Thermique, Energetique et Procedes – IPRA, EA 1932, Rue Jules Ferry - BP 7511 - 64075 PAU Cedex

*corresponding author: erwin.franquet@univ-pau.fr

Abstract – Thermal energy storage systems based on phase change materials are interesting candidates to handle the difficulties raised by intermittent renewable sources or by batch processes. Among these systems, many rely on the use of steam, as for instance in concentrating solar power plants or district heating, or in the pharmaceutical or food industries. Today, there is no systematic method to design such systems quickly and easily since complex heat transfer is observed due to the influence of the geometry and to the dual characteristics associated with solid/liquid and liquid/gas transitions. The aim of the present work is thus to propose a multi-scale modelling methodology of a latent heat storage system for the storage of steam. It mainly involves two different simulation models with different scales for the heat transfer fluid and the phase change material. Furthermore, it relies on the use of a heat transfer correlation based on specific non-dimensional numbers, which is deduced from previous simulations of the phase change material's behavior, obtained with fine 3D computational fluid dynamics calculations. Consequently, a reduced model is built to simulate the whole system. This model does not need to be tuned against experiments. This model is then directly used to compare the numerical results with measurements coming from a prototype scale latent heat storage available at CEA Grenoble. The results are very promising and show that an *a priori* approach that is more physically consistent and not based on any model tuning can lead to acceptable results. Moreover, the computational time can be divided by 10 to 40, thus allowing future design and real performance evaluations of latent heat storage modules.

Keywords – Thermal energy storage; liquid-vapor; solid-liquid; model reduction; non-dimensional correlation; heat transfer

Highlights

- Development of a reduced multi-scale modelling approach for the charge of a steam storage module involving a PCM.
- Deduction of a heat transfer correlation from fine 3D CFD computations.
- No experimental tuning.
- Dual two-phase storage with liquid/gas HTF inside the tubes and solid/liquid PCM outside.
- A local heat transfer correlation is built.

© 2020 published by Elsevier. This manuscript is made available under the CC BY NC user license
https://creativecommons.org/licenses/by-nc/4.0/

Nomenclature

Latin letters

A	factor in the damping term of the momentum equation ($kg.m^{-3}.s^{-1}$)
A_{mush}	mushy zone constant ($kg.m^{-3}.s^{-1}$)
b	constant term in the damping term
c	tube perimeter (m)
c_p	heat capacity at constant pressure ($J.kg^{-1}.K^{-1}$)
D	thermal diffusivity ($m^2.s^{-1}$)
e_l	liquid layer thickness (m)
g, $\vec{g}$	acceleration of gravity ($m.s^{-2}$)
h	mass enthalpy ($J.kg^{-1}$)
l_c	characteristic length (m)
L	latent heat ($J.kg^{-1}$)
$\dot{m}$	mass flow-rate ($kg.s^{-1}$)
Nu	Nusselt number (–)
P	pressure (Pa)
r	radial coordinate (m)
R	radius (m)
Ra	Rayleigh number (–)
S	tube section (m^2)
S_e	heat exchange surface (m^2)
t	time (s)
T	temperature (°C or K)
$\vec{U}$	velocity ($m.s^{-1}$)
V	volume (m^3)
x	volume fraction (–)
Y	mass fraction (–)
z	axial coordinate (m) (–)

Greek symbols

α	heat transfer coefficient ($W.m^{-2}.K^{-1}$)
β	thermal expansion coefficient (K^{-1})
ρ	density ($kg.\ m^{-3}$)
μ	dynamic viscosity ($kg.\ m^{-1}.s^{-1}$)
ν	kinematic viscosity ($m^2.s^{-1}$)
ε	void fraction (–)
λ	thermal conductivity ($W.m^{-1}.K^{-1}$)
λ_{eq}	equivalent thermal conductivity ($W.m^{-1}.K^{-1}$)
φ	heat flux ($W.m^{-2}$)
ϕ	heat flow-rate (W)

Superscript and subscripts

$\overline{A}$	mean value of A
eff	effective

ext	external boundary
fin	fins and inserts
h	homogeneous material
i, j	cell indexes (axial and radial direction)
l	liquid phase
liq	liquidus
pc	phase change
ref	reference
s	solid
sat	saturation
sens	sensible
sol	solidus
t	tube
text	outer tube wall
tint	inner tube wall
v	vapor phase
w	wall

1

2 Abbreviations

CSP	concentrated solar power
DSG	direct steam generation
HTF	heat transfer fluid
LHS	latent heat storage
PCM	phase change material

3

1 Introduction

1.1 Forewords

Thermal energy storage systems are known to be key components of solar thermal power plants, principally because they reduce the probabilities of breakdown [1], [2] and thus lead to more stable regimes. At the same time, many industrial applications make a huge use of steam, as for example in Direct Steam Generation (DSG) concentrating solar power (CSP) plants, where the two-phase heat transfer fluid (HTF) avoids the installation of heat exchangers and extends the 400°C limit usually associated with common thermal oils. Again, this simplifies the design and operations, and increases overall efficiency [3], [4]. Nonetheless, the thermal storage of DSG-CSP must be adapted to the two-phase feature of the HTF. Generally, a steam accumulator is used and the water vapor is stored in pressurized vessels, in a saturated state in thermal equilibrium with a saturated liquid water volume [5]. Unfortunately, such technologies are rather expensive when large capacities are needed [6], [7]. Therefore, the underlying research question of the present contribution concerns the development of latent heat storages (LHSs), using phase change materials (PCMs) to store the thermal energy of the steam in the latent heat of a solid-liquid phase transition. In such storage systems where the phase change occurs in a narrow temperature range, the steam pressure drop between charge and discharge cycles is minimized compared to sensible storages [8]. The most mature steam storage technology with PCM is the shell-and-tube concept [9], [10], where the HTF flows in tubes that go through a PCM-filled tank. During the charge, the steam condenses inside the tubes and the initially solid PCM progressively melts, while during the discharge, liquid water fed to the tubes evaporates and regenerates steam due to the heat released during the solidification of the PCM. Practically, metallic or graphite fins are often disposed around these tubes to enhance the heat transfer, in order to cope with the low thermal conductivities of usual PCM [11]. Moreover, the PCM shell does not need to be pressurized, which simplifies the storage design and reduces its costs. Generally, there are two materials that are regularly used as PCMs with storages designed for CSP applications, namely sodium nitrate $NaNO_3$ [6]-[8], [12], [20] and a eutectic mixture of potassium nitrate and sodium nitrate $KNO_3/NaNO_3$. [11], [14]. For prototypes or laboratory scale bench-top modules, all kinds of PCM can be found, such as for instance RT35-HC [9]-[10] or n-octadecane [16]-[17], as well as salt hydrates [19]. Several prototype-scale shell-and-tube LHS modules involving a two-phase liquid water – steam HTF have been built and successfully operated by several teams around the world [6], [12], [92], demonstrating the feasibility and the relevance of this concept for the storage of steam. Among numerical studies, a few 1D or 2D simulation models intended for module design or quick performance estimation can be found in the literature [7], [8], [20]. Due to the small number of large-scale modules being built, and to the complexity of the heat transfer phenomena inside a module, no design model has yet been validated on experimental data from large-scale modules. In summary, since the selection of a PCM is known to be strongly oriented by the storage application, DSG-CSP plants require a PCM whose phase transition is around 300°C (saturation temperature of steam at a pressure level suitable for turbine operations). In this temperature range, inorganic salts (such as sodium nitrate) are an interesting solution thanks to their favorable physical and chemical properties (stable, non-corrosive) and low cost. Their major drawback is their low thermal conductivity, which implies either very low charging and discharging thermal powers, or a small distance between tubes. To achieve acceptable charge and discharge times (typically about six hours for CSP applications), without increasing the number of tubes and thus the cost of the heat exchanger, an improvement in the heat transfers is needed.

In general, the heat transfer coefficient between the condensing/evaporating HTF and the inner tube wall is high. Consequently, the heat transfer dynamics are mainly driven by the phenomena occurring on the PCM side. Here, heat transfer is influenced by both the geometric shape and dimensions of the fins, and by the possible natural convection movements inside the PCM liquid phase. Indeed, several studies have shown that natural convection could have a non-negligible influence on the thermal performances of a storage module [12]–[15]. Since computational fluid dynamics (CFD) calculations, which are capable of representing this kind of problem, are often too long and/or expensive, one needs simpler engineering tools to perform fast and multiple computations. Generally, one tries to rely on heat transfer correlations [16]-[17]; however, these correlations often lack generality and show caveats when they are simply fitted on experimental data [16]–[19]. In contrast, other studies propose to use CFD simulations to estimate

a non-dimensional correlation, which can then be used later on in a reduced system model. Thus, Garcia *et al.* [12] and Johnson *et al.* [20] implemented such a technique in a 3D purely conductive regime of fusion/solidification to account for the role of fins and inserts. Another similar approach can be found in Mostafavi Tehrani *et al.* [21] who modeled the convective-driven melting of a PCM around a single tube without fins and inserts. They deduced from these simulations a non-dimensional correlation for the heat transfer, which was then used in a reduced system model. In fact, the underlying goals of these analyses are to allow for better predictions of the main features of the storages, namely their energy capacity and associated efficiency and their charging/discharging times. These characteristics are of paramount importance, yet they are singularly different from one case to another. For instance, in [6, 99] a $NaNO_3$-based storage system with an average storage capacity of 700 kWh and a discharge thermal power of 200 to 500 kW was investigated both experimentally and numerically. Its charging time was around 1-3h. The same PCM, with the same methodology, were used in the LHASSA module [12] where full cycles for the charge and discharge lasted approximately 8 h and 6 h respectively, with a storage efficiency of 90%. The equivalent powers were thus around 35 kW and 47 kW. Along the same lines, [97] performed a numerical study of the effectiveness of a multi-tube storage, with a NaCl-$MgCl_2$ eutectic mixture as a PCM, where the length and diameter were varied (between 10 to 150 m, and between 1 and 2 inches and 1 and 2 and 3 inches for the inner diameter of the tubes and the space between them). Results showed a variation in the efficiency of the order of 70%. With an insulated steel container housing a fin-tube heat exchanger filled with HDPE, [96] demonstrated experimentally and numerically the achievement of a 20-25 kWh storage in 1-2 h. In the case of smaller volumes or with preliminary prototype modules, the same research questions regularly arise. In [98], three 0.5 m concentric tubes with internal fins containing a tube with internal fins, and PCM between them, was experimentally investigated, to show that charging could occur in 60 to 160 min. In [15], concentric tubes, with varying lengths and radii for the PCM zone, were tested together with three different PCM (H325, H425 and H525). Whatever the PCM, the charging (respectively discharging) time was shown to vary up to three (resp. 2) times depending on the conditions, while the maximum variation between the various PCM could go up to six in both modes. In [19], a prototype of a 140 L shell-and-tube storage permitted to measure a 5 kW power charge and 2-3.5 kW power discharge with RT70, and a 3.55 kW power charge and 2-3 kW power discharge with $MgCl_2{\cdot}6H_2O$. Lastly, an interesting concept of a new fin design, for a shell containing extended finned tubes surrounded by $NaNO_3$ as PCM, was simulated in [20]. The discharge thermal power per tube length varied from 3 to 10 kWm^{-1}, to fulfill the 15 min constraint initially set in their project.

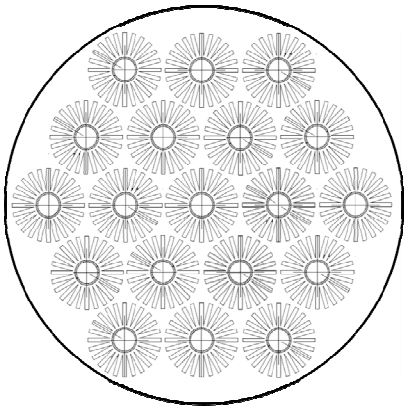
1.2 Novelty of the study

This work presents the development of a reduced multi-scale modelling approach for the charge of a steam storage module involving a PCM. Similarly to what was proposed by Mostafavi Tehrani *et al.* [21], a heat transfer correlation during the melting is deduced on the PCM side from fine 3D CFD computations. Indeed, as it is judiciously highlighted in [sec. 1.2 p. 4, 21], prior correlations too often rely on experimental fitting. The contributions of this paper are threefold. First, it proposes to continue apace the development of such a methodology since it has the potential to avoid any experimental tuning and to overcome the limits of corresponding methods. In fact, the implicit goal is to further improve the knowledge concerning heat transfer correlations for solid/liquid phase change, since it still lags far behind what can be found for liquid/gas phase change, e.g. [33]. Secondly, to the authors' knowledge, this is the first time ever that such a method is used for multi-tubes with fins and inserts, and for a dual two-phase storage with liquid/gas HTF inside the tubes and solid/liquid PCM outside. Thirdly, a local correlation is built, and not an average one. Since phase changes, from both the HTF and PCM, can occupy only part of the tube's length, the heat transfer is indeed far from being homogeneous. Here again, this is the first time that such a procedure is considered.

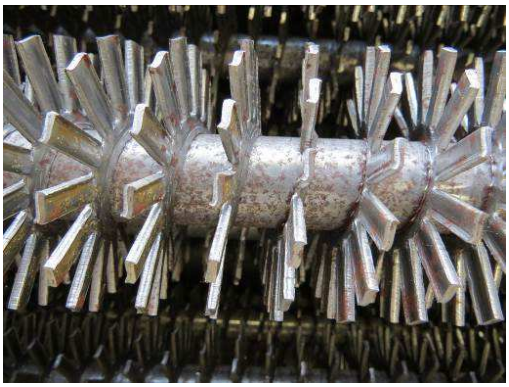
2 Methodology

As stated above, the current situation deals with a prototype shell-and-tube latent heat steam storage module available at CEA Grenoble [93, 95]. This module is made of a cylindrical shell, containing a bundle of 19 finned tubes (see Figure 1-(a)), with melded rectangular fins following a helical pattern (see Figure 1-(b)). This storage design does not include any inserts. Both tubes and fins are made of carbon steel SA334 Grade 6. To be cost competitive, storage

modules are designed using off-the-shelf standard fins. The closer the tubes or the higher the heat exchange surface of the fins, the higher the thermal performances of the storage system and the higher its cost: consequently, the spacing between the tubes is logically a trade-off between system performances and costs. The HTF flows inside the tubes, whereas the shell is filled with approximately 1700 kg of sodium nitrate ($NaNO_3$). The immerged tube length is 4.08 m when the PCM is fully liquid.



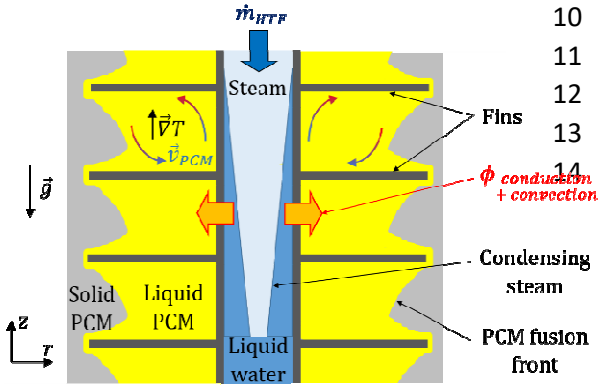
(a) tubes bundle distribution (black circle represents the outer shell of the module)



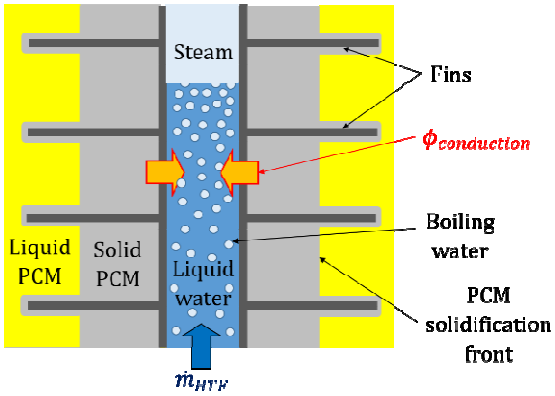
(b) side photograph of the finned tubes

Figure 1: Description of the prototype storage module

Schematically, the present problem is summarized in Figure 2. The two-phase HTF (liquid water / steam) and the PCM (solid / liquid) exchange heat and three thermal resistances can be identified, which need to be assessed. First, a convective heat exchange takes place between the flowing HTF and the inner tube wall. Second, the heat flow goes through the tube wall by thermal conduction. Third, heat is exchanged between the external tube wall and the PCM, either by the fins or directly at the tube's surface. Generally, the main difficulty comes from this last thermal resistance, involving the PCM, and, consequently, this will be one of the cornerstones of the present paper.



(a) charge



(b) discharge

Figure 2 : Schematic view of the physical phenomena occurring in a shell-and-tube steam storage system based on LHS

Firstly, a 3D CFD model is used to simulate the phase transition of the PCM, in presence of conductive and convective heat transfer. Then, several simulations are performed to build a non-dimensional correlation for the heat transfer, considering both the presence of fins and the phase change. Following the classic approach for non-reactive convective-only flows, this correlation is searched under the following form [22], [23]:

$$\boxed{Nu = C\,Ra^{n}} \qquad (1)$$

Here, the Rayleigh and Nusselt numbers need to be properly defined, since their expression is not unequivocal [24], [16], [17], [25], [21], [26]:

$$Ra = g\left(\frac{\beta}{\nu D}\right)_{PCM}(T_w - \bar{T}_{PCM}){l_c}^3 \quad (2)$$

$$Nu = \frac{\phi}{S_e(T_w - \bar{T}_{PCM})}\frac{l_c}{\lambda_{PCM,l}} \quad (3)$$

There are indeed various possible definitions for the characteristic length l_c and the mean PCM temperature $\bar{T}_{PCM}$. Besides, these definitions must be local since a local correlation is searched for; so, they should involve the altitude inside the tube. Several possibilities will be discussed and compared, as shown in section 3.2.

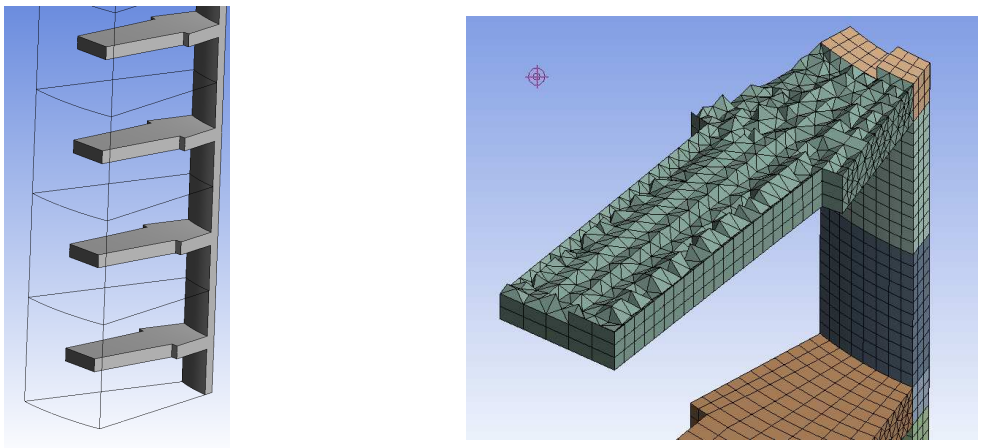
Secondly, a reduced system model is built to represent the whole dual two-phase storage module. The goal being to develop a fast and stand-alone tool, the outside of the tube (PCM, fins, inserts if any) is approximated as a homogeneous material, and natural convection inside the PCM is handled through an effective thermal conductivity. Practically, this latter is based on the previous Nusselt correlation, built from prior numerical experiments with the previous CFD model.

Eventually, the proposed methodology was then used for the prototype shell-and-tube latent heat steam storage module presented in Figure 1, to carry out three simulations of charging mode.

3 Determination of the heat transfer correlation

3.1 CFD modelling

In the present calculations, for the sake of limiting the computational time, only an angular sector of 22.5° and a tube length of 0.54 m (27 fins) are represented (see Figure 3-(a)). For the associated boundary conditions, a fixed temperature is set at the inner tube wall and a symmetry condition for the lateral and outer boundaries, while a wall condition is imposed for the others. The entire mesh is composed of 539 046 cells, whose mean size is 0.83 mm, and its maximum skewness is 0.81 (see Figure 3-(b)). Grid independence was verified by comparing punctual PCM temperature evolutions at several distances from the external tube wall to those obtained with a finer mesh containing 774 098 cells, for a mean size of 0.63 mm. The coarser mesh was found to give acceptable results, and furthermore, its features are similar to those used in [14-15]. The time step adopted is 0.025 s or 0.05 s, depending on the simulations, and, here again, the independence of the results on the time step was checked by dividing it regularly by 2.



a) fraction of the prototype simulated (b) details of the mesh in the wall and fins

Figure 3 : Description of the geometry and mesh retained

Next, the PCM is modelled using the enthalpy-porosity approach, described by Voller and Prakash [30], which assumes an incompressible regime and uses the Boussinesq approximation to account for the buoyancy forces. The balance equations for mass, momentum and energy conservations are written:

$$\vec{\nabla} \cdot \vec{U} = 0 \quad (4)$$

$$\rho\left(\frac{d\vec{U}}{dt}+\vec{U}\cdot\vec{\nabla}\vec{U}\right)=-\vec{\nabla}P+\vec{\nabla}\left(\mu\vec{\nabla}\vec{U}\right)-\rho\beta\left(T-T_{ref}\right)\vec{g}+A\vec{U} \quad (5)$$

$$\rho c_p\left(\frac{dT}{dt}+\vec{U}\cdot\vec{\nabla}T\right)=\vec{\nabla}\left(\lambda\vec{\nabla}T\right)-\rho L\left(\frac{dY_l}{dt}+\vec{U}\cdot\vec{\nabla}Y_l\right) \quad (6)$$

The porosity approach consists in adding a damping term at the end of the right-hand side of the momentum equation, whose role is to cancel the velocity field in solid phase. It expresses:

$$A=-A_{mush}\frac{(1-Y_l)^2}{{Y_l}^3+b} \quad (7)$$

with $b = 10^{-3}$.

In the tube wall and fins, only the energy equation applies:

$$\rho c_p\frac{\partial T}{\partial t}=\lambda\Delta T \quad (8)$$

The physical properties of the PCM and the steel are given in Table 1, and in Figure 4 and Figure 5. The value of the mushy zone constant was set to $A_{mush} = 10^8$ kg.m^{-3}.s^{-1}, using a prior experiment where the temperature field was compared with corresponding measurements [93, 94]. For the specific heat capacities and the thermal conductivities, linear regressions were performed.

Table 1: Material properties for the CFD model

Material	$NaNO_3$ [9], [10],[31],[32]	Steel
ρ (kg.m^{-3})	1927	7764
β (K^{-1})	3.8 10^{-4}	--
c_p (J.kg^{-1}.K^{-1})		
solid	Variable	542.8
liquid	1704	
λ (W.m^{-1}.K^{-1})		
solid	Variable	50.33
liquid	Variable	
μ (Pa.s)	2.8 10^{-3}	--
L (kJ.kg^{-1})	173.3	--
T_{sol} (°C)	303.3	--
T_{liq} (°C)	306.6	--

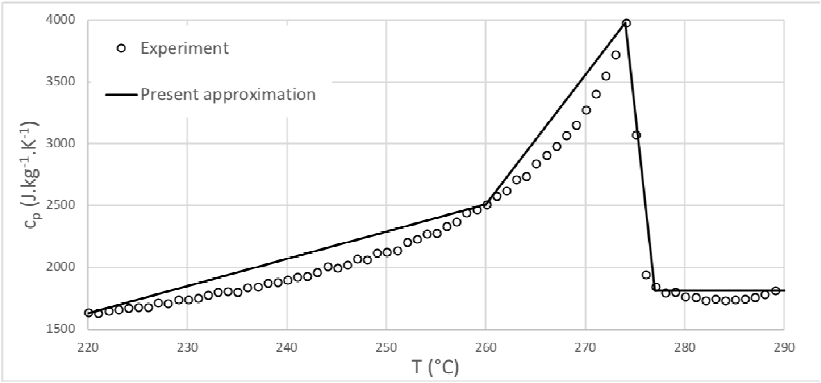


Figure 4 : Specific heat capacity of $NaNO_3$

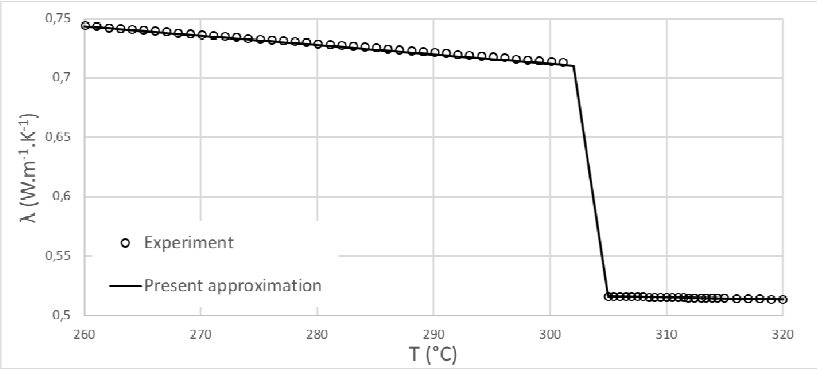


Figure 5 : Thermal conductivity of $NaNO_3$

The numerical experiments were performed with ANSYS Fluent® v. 17.2 software. Due to the incompressible feature of the partial differential equations system (4-6), a pressure-based formulation was chosen. Then, the PISO scheme was adopted for the pressure-velocity coupling together with, respectively, a second order upwind scheme for the convective terms in the momentum and energy equations and a least-square cell-based scheme for the diffusive terms. Finally, the pressure equation was discretized with the PRESTO! approach; for the residuals' convergence, relative decrease values of 10^{-3} were taken for the continuity and momentum equations but the energy residual was set to 10^{-11} [91].

3.2 Non-dimensional relation

Three CFD computations were performed with an imposed temperature T_w = 310, 318 and 328°C respectively at the inner tube wall. The PCM is initially solid at 290°C. The meshed domain was then divided into 27 *representative volumes*, centered on the individual fins (the boundaries between these volumes can be seen on Figure 3-(a)). Regularly, the heat flow-rate entering the PCM was recorded as a function of time, along with associated physical variables, *e.g.* temperature field, molten fraction…

From these values, expressions were investigated for the characteristic length l_c and the mean PCM temperature $\overline{T}_{PCM}$ involved in Eqs. (2-3). Thus, four and three different relations were tested for l_c and $\overline{T}_{PCM}$ respectively:

- Characteristic length l_c
  1. Altitude, taken at the center of the representative volume considered:

$$l_c = z_i \tag{9}$$

  2. Thickness of the annular space outside the tube:

$$l_c = R_{ext} - R_{text} \tag{10}$$

  3. Local thickness of the liquid PCM layer:

$$l_c = -R_{ext} + \sqrt{{R_{ext}}^2 + \left({R_{text}}^2 - {R_{ext}}^2\right)\overline{Y_{l,i}}} \tag{11}$$

  where $\overline{Y_{l,i}}$ is the mean mass liquid fraction in the representative volume considered:

$$\overline{Y_l} = \frac{\sum_{i=1}^{nb\ PCM\ cells} \rho_i Y_{l,i} V_i}{\sum_{i=1}^{nb\ PCM\ cells} \rho_i V_i} \tag{12}$$

  4. Present complete thickness of the liquid PCM layer on the whole tube height:

$$l_c = -R_{ext} + \sqrt{{R_{ext}}^2 + \left({R_{text}}^2 - {R_{ext}}^2\right)\overline{Y_l}} \tag{13}$$

where $\overline{Y_l}$ is computed in the same way as $\overline{Y_{l,i}}$, but by averaging the liquid fraction on the whole computational domain, and not only on the representative volume considered.

- Mean PCM temperature $\overline{T}_{PCM}$

1. Phase change temperature:

$$\overline{T}_{PCM} = T_{pc} = \frac{1}{2}\left(T_{sol} + T_{liq}\right) \quad (14)$$

2. Mean temperature of the liquid PCM layer in the representative volume considered:

$$\overline{T}_{PCM} = \frac{\sum_{i=1}^{nb\ PCM\ cells} c_{p,i} T_i Y_{l,i} V_i}{\sum_{i=1}^{nb\ PCM\ cells} c_{p,i} Y_{l,i} V_i} \quad (15)$$

3. Temperature of the first mesh cells near the outer tube wall. It is computed as the mean temperature of six PCM cells and one fine mesh cell near the wall, as shown on Figure 6.

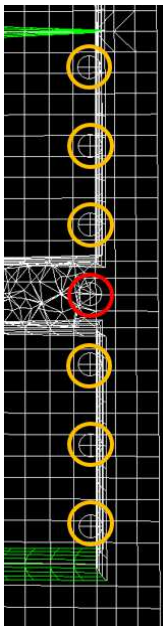
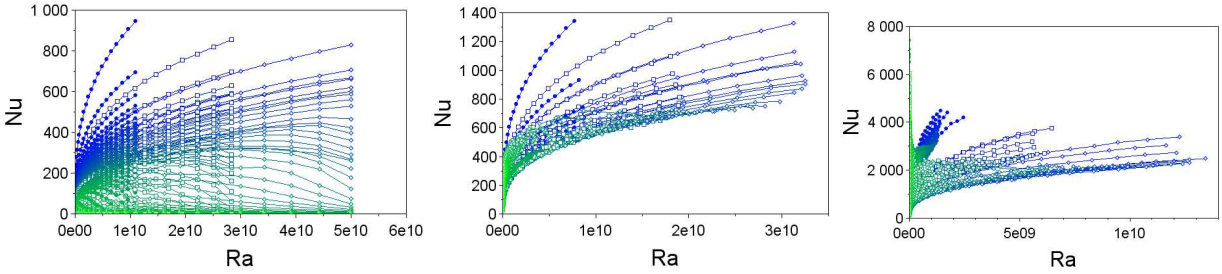
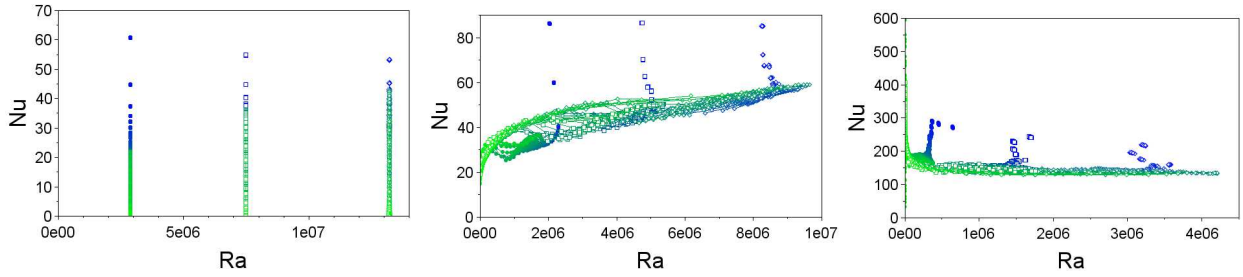


Figure 6: Mesh cells near the outer wall of the inner tube (yellow: PCM cells; red: fin cells)

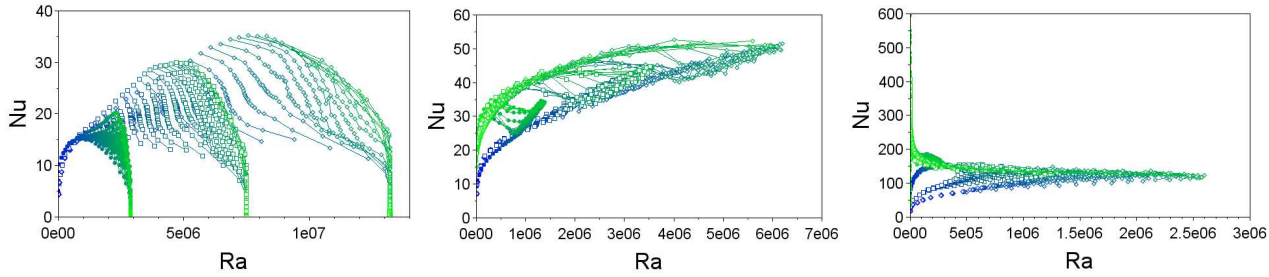
This enabled 12 scatter plots to be drawn, to assess whether or not the above expressions allow the Rayleigh and Nusselt numbers to correlate. The corresponding graphs are shown in Figure 7. From the results available on Figure 7, one can easily note that some definitions for the characteristic length l_c and the mean PCM temperature $\overline{T}_{PCM}$ do not lead to a good correlation between the Rayleigh and Nusselt numbers. This is especially the case for Eq. (14), whatever the definition of l_c, and similarly for Eq. (9), whatever the definition of $\overline{T}_{PCM}$. For the six remaining candidates, two behaviors can be observed. Either the points gather relatively well around a single curve, except at the beginning of melting, or two curves are to be found (one for the lowest Nusselt numbers at the beginning of melting – in blue –, and then another one for the highest Nusselt numbers at the end of melting – in green –). Given that the heat transfer should go from a mainly conductive regime to a convection-dominated one, it is preferable to select the latter case. Therefore, one can use either Eqs. (11) or (13) for the characteristic length l_c and the mean PCM temperature $\overline{T}_{PCM}$ should be taken as that of the liquid layer Eq. (15) at the given height.



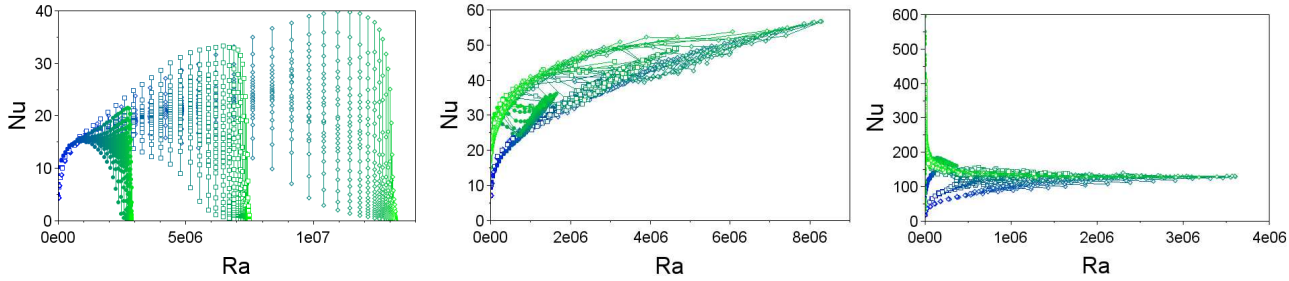
(a) Characteristic length given by Eq. (9)



(b) Characteristic length given by Eq. (10)



(c) Characteristic length given by Eq. (11)



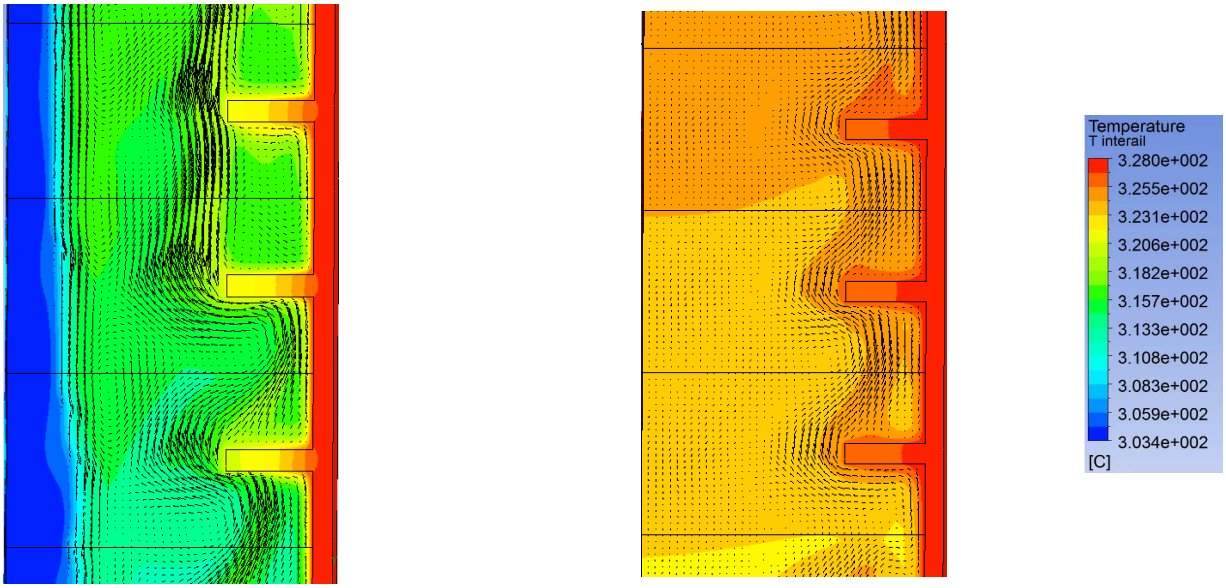
(d) Characteristic length given by Eq. (13)

Figure 7: Accuracy of the correlation between the Rayleigh and Nusselt numbers depending on the definitions taken for $\overline{l_c}$ and $\overline{T_{PCM}}$: phase change temperature (left), mean liquid temperature at the considered height (middle), mean temperature near the wall (right)

To further highlight this difference between low and high Nusselt numbers, for a given similar Rayleigh number, it is proposed to look at the temperature and velocity fields at a time when the 27 representative volumes are split between both curves. Figure 8 presents the corresponding results in these two zones, in a vertical plane situated in the middle of the domain. Depending on the vertical position in the tube, the Nusselt number can either undergo small values, corresponding to a velocity maximum at 17 mm.s^{-1} (see Figure 8.a), or high values, for an equivalent maximum velocity at 9 mm.s^{-1} (see Figure 8.b).

Then, it can be noted that melting is still ongoing in volumes whose (*Ra*, *Nu*) values gather around the first curve, whereas melting of the PCM is complete in volumes whose (*Ra*, *Nu*) couples follow the second curve. Besides, one can remark the highest velocity magnitudes in the first case. This is due to the higher temperature gradient inside the PCM, between the phase front remaining at the melting temperature and the inner wall (also at a fixed temperature).

When the PCM is molten, heat transfer is singularly reduced since this temperature gradient is reduced. Finally, these two situations just entail two different regimes of convective heat transfer, logically associated with two different scaling laws. Last but not least, it was verified that points lying between these two asymptotic behaviors show liquid fraction values between 0 and 1 at the external boundary of the domain.



(a) lower portion of the tube with ongoing melting

(b) higher portion of the tube where fusion is over (only liquid phase here)

Figure 8: Temperature and velocity fields at t = 2390 s for the case T_w = 328°C

In summary, using Eqs. (11) or (13) and Eq. (15) for, respectively, the characteristic length l_c and the mean PCM temperature $\overline{T}_{PCM}$ gives to obtain a scaling law between the Nusselt and Rayleigh numbers. Depending on the time and the altitude, that is to say depending on the completeness of the phase change, this scaling law will be bounded by two asymptotic behaviors. In this respect, a local heat transfer correlation will be preferred for Eq. (1) and, consequently, final choices will rely on Eqs. (11) or (15). It leads to the following scaling laws for the two limiting cases:

$$Nu = 0.402\ Ra^{0.306} \tag{16}$$

$$Nu = 2.614\ Ra^{0.196} \tag{17}$$

As can be seen on Figure 9, a very good agreement with the numerical results is observed.

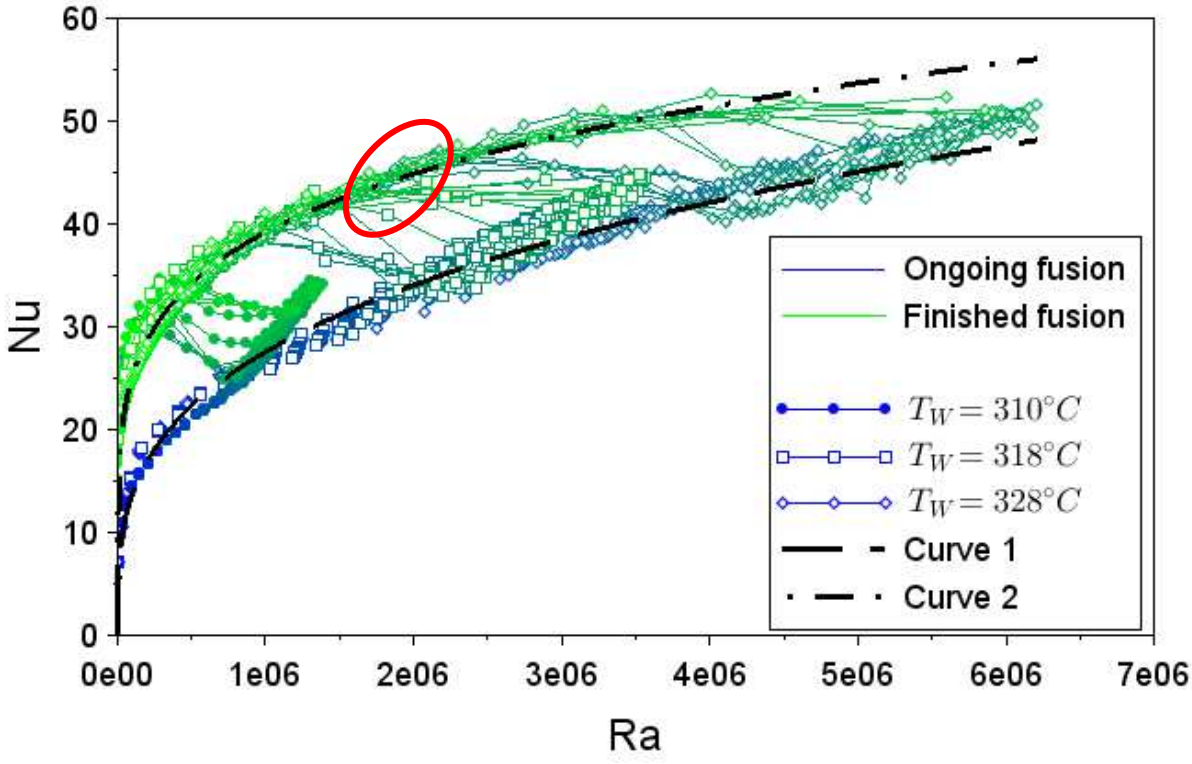


Figure 9: Comparisons of the (Ra, Nu) scatter plot obtained from the CFD results, using Eqs. (11) and (15) for the definitions of l_c and T_{PCM}, with correlations (16) and (17) for the heat transfer

From a practical point of view, one will need a criterion to know when to go from one expression to the other. Indeed, a continuous formulation is required since the real physical heat transfer is not discontinuous and, second, because it is more suitable in a reduced model to avoid oscillations and unstable behaviors. As the proper definition of this threshold is beyond the scope of the present article, the following definition was chosen:

$$\begin{cases} Nu_i = 0.402\ Ra_i^{0.306} & 0 < \overline{Y_{l,i}} < 0.98 \\ Nu_i = \dfrac{\overline{Y_{l,i}} - 0.98}{0.02}\left(2.614\ Ra_i^{0.196}\right) + \dfrac{1 - \overline{Y_{l,i}}}{0.02}\left(0.402\ Ra_i^{0.306}\right) & 0.98 < \overline{Y_{l,i}} < 1 \\ Nu_i = 2.614\ Ra_i^{0.196} & \overline{Y_{l,i}} = 1 \end{cases} \quad (18)$$

4 Application

As mentioned in Section 2, the idea is now to use the Nusselt correlation thus obtained to build an effective thermal conductivity that can be implemented in the reduced model, as summarized in Figure 10. The proposed methodology will be tested on the three previous fusion experiments.

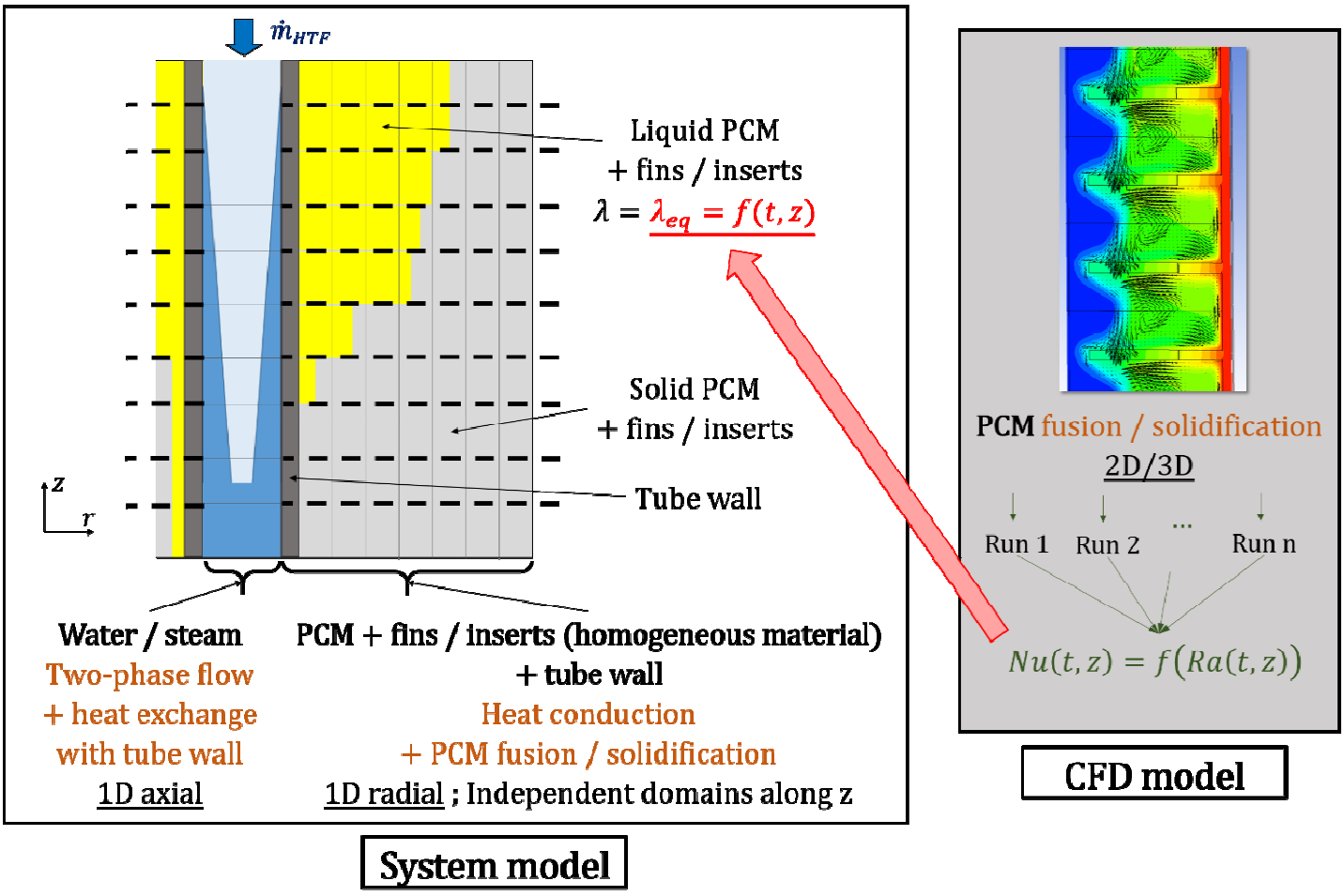


Figure 10 : Structure and characteristics of the proposed multi-scale model

4.1 System modelling

The present model will stand for the two-phase HTF inside the tube, for the tube, and for the fins, inserts and PCM approximated together as a homogeneous material. For each of these materials, 1D and 2D discretization are adopted respectively.

On the HTF side, the flow has been shown to be in forced regime [10]. Moreover, the liquid and vapor phases are assumed to be in thermal and dynamical equilibrium, *i.e.* with the same local velocity and temperature, and axial conduction is neglected. Therefore, the PDE system for the HTF, incorporating directly the wall boundary condition in the energy equation [28], is written:

$$S_{tint}\frac{\partial \rho_{HTF}}{\partial t} + \frac{\partial \dot{m}}{\partial z} = 0 \tag{19}$$

$$S_{tint}\rho_{HTF}\frac{\partial h_{HTF}}{\partial t} + \frac{\partial (\dot{m}\, h_{HTF})}{\partial z} - c_{tint}\varphi_{tint} = 0 \tag{20}$$

To compute the HTF density, it is assumed that liquid and vapor phases are at saturation in the two-phase region:

$$\rho_{HTF} = \varepsilon \rho_{HTF,v}^{sat} + (1-\varepsilon)\rho_{HTF,l}^{sat} \tag{21}$$

with

$$\varepsilon = \frac{1}{1 + \frac{1 - Y_{HTF,v}}{Y_{HTF,v}}\frac{\rho_{HTF,v}^{sat}}{\rho_{HTF,l}^{sat}}} \tag{22}$$

$$Y_v = \frac{h_{HTF} - h_{HTF,l}^{sat}}{h_{HTF,v}^{sat} - h_{HTF,l}^{sat}} \tag{23}$$

Finally, the heat flux at the wall is calculated by means of a classic thermal resistance:

$$\varphi_{tint} = \frac{T_t - T_{HTF}}{\frac{1}{\alpha_{HTF}} + \frac{R_{tint} \ln\left(\frac{1}{2} + \frac{R_{text}}{2\,R_{tint}}\right)}{\lambda_t}} \tag{24}$$

Next, the tube simply obeys the heat equation. Following the thermal resistance analogy of Eq. (24), the energy balance is written (using enthalpy for the sake of clarity with other PDE systems):

$$S_t \rho_t \frac{\partial h_t}{\partial t} = S_t \lambda_t \frac{\partial^2 T_p}{\partial z^2} + c_{text}\varphi_{text} - c_{tint}\varphi_{tint} \tag{25}$$

and logically, one gets for the outer heat flux:

$$\varphi_{text} = \frac{T_h - T_t}{R_{text}\left(\frac{\ln\left(\frac{2\,R_{text}}{R_{tint} + R_{text}}\right)}{\lambda_t} + \frac{\ln\left(1 + \frac{\Delta r}{2\,R_{text}}\right)}{\lambda_{h,\mathrm{eq}}}\right)} \tag{26}$$

Last but not least, one needs to write the modelling of the homogeneous material. Since natural convection is accounted for by means of an effective thermal conductivity, it only relies on the energy balance equation. To handle the latent term, the previous source term approach [29] is still considered. For the sake of simplicity, the heat transfer in the axial direction is neglected and thermal losses are also assumed to be negligible. Thus, the energy equation can be written:

$$\rho_h \frac{\partial h_{h,sens}}{\partial t} = \lambda_{\mathrm{h}}\left(\frac{\partial^2 T_h}{\partial r^2} + \frac{1}{r}\frac{\partial T_h}{\partial r}\right) - \rho_{PCM} x_{PCM} L \frac{\partial Y_{PCM,l}}{\partial t} \tag{27}$$

where the average properties are given by:

$$\rho_h = x_{PCM}\rho_{PCM} + (1 - x_{PCM})\rho_{fin} \tag{28}$$

$$c_{p,h} = Y_{PCM} c_{p,PCM} + (1 - Y_{PCM}) c_{p,fin} \tag{29}$$

Then, the paramount parameter that needs to be further detailed is the effective thermal conductivity. It is generally deduced from the Nusselt number, or equivalently, from the Rayleigh number. During melting, the situation encountered can be represented as depicted in Figure 11: thermal conductivity of the homogeneous material corresponds to the effective thermal conductivity λ_{eff} in the liquid molten layer and to the average thermal conductivity in the external solid part.

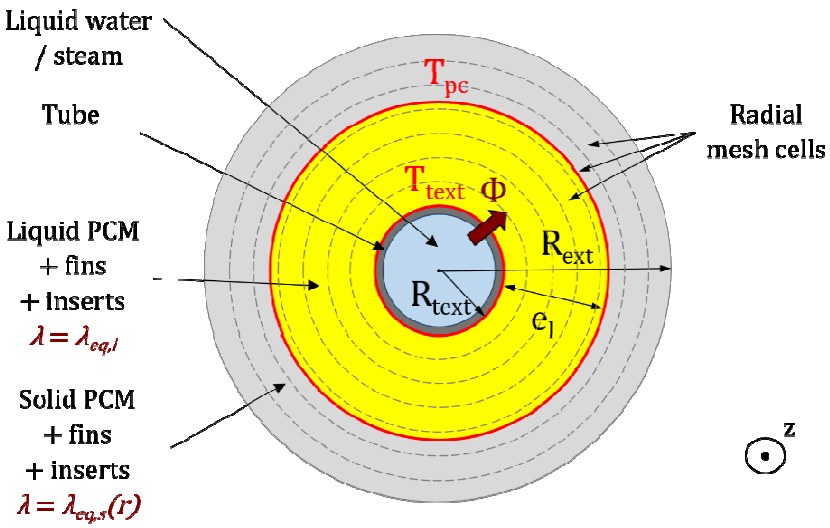


Figure 11: General case for the definition of the effective thermal conductivity

By definition, the effective thermal conductivity is such that the total amount of heat is equal to the heat exchanged in the convective case:

$$\phi = 2\pi\Delta z\lambda_{\mathrm{eq},l}\frac{\left(T_{text}-T_{pc}\right)}{\ln\left(1+\frac{e_l}{R_{text}}\right)} \tag{30}$$

To express the thickness of the liquid layer e_l, a mass balance is used, involving the mean mass liquid fraction at the considered altitude $\overline{Y_l}$:

$$e_l = -R_{text} + \sqrt{R_{text}^2 + (R_{ext}^2 - R_{text}^2)\overline{Y}_l} \tag{31}$$

$$\overline{Y}_l = \frac{\sum_{j=1}^{nb\ mesh\ cells,sub-domain} Y_{l,j}\rho_{PCM}x_v V_j}{\sum_{j=1}^{nb\ mesh\ cells,sub-domain} \rho_{PCM}x_v V_j} \tag{32}$$

In (32), V_j represents the volume of the j-th cell in the radial direction.

Then, at a given altitude z along the tube, the local Nusselt and Rayleigh numbers are expressed as follows:

$$Nu(z) = \frac{\phi}{2\pi R_{text}\Delta z(T_{text}(z)-T_{PCM}(z))}\frac{l_c(z)}{\lambda_{PCM,l}} \tag{33}$$

$$Ra(z) = g\left(\frac{\beta}{\nu D}\right)_{PCM}\left(T_{text}(z)-T_{PCM}(z)\right)l_c(z)^3 \tag{34}$$

By combining equations (30), (31), (33) and (34), one gets:

$$\lambda_{\mathrm{eq},l}(z) = \lambda_{PCM,l}\frac{T_{text}(z)-T_{PCM}(z)}{T_{text}(z)-T_{pc}}\frac{R_{text}}{l_c(z)} \times \ln\left(1+\frac{-R_{text}+\sqrt{R_{ext}^2+(R_{ext}^2-R_{text}^2)\overline{Y}_l(z)}}{R_{text}}\right) \times f\left(g\left(\frac{\beta}{\nu D}\right)_{PCM}(T_{text}(z)-T_{PCM}(z))l_c(z)^3\right) \tag{35}$$

In the solid part, a classic mean calculation holds:

$$\lambda_{eq,s,j} = Y_{PCM,s,j}\lambda_{PCM,s} + \left(1-Y_{PCM,s,j}\right)\lambda_{fin} \tag{36}$$

Finally, in each cell, the equivalent thermal conductivity $\lambda_{eq,j}$ is computed with a weighted sum between the effective thermal conductivity in the liquid layer and the homogeneous equivalent thermal conductivity in the solid layer:

$$\lambda_{eq,j} = Y_{l,j}\lambda_{\mathrm{eq},l} + \left(1 - Y_{l,j}\right)\lambda_{eq,s,j} \tag{37}$$

The values of all the other variables, and of the operational parameters, are provided in Table 2.

Table 2: Material and operational properties for the system model

Geometrical configuration	
Total PCM volume fraction	0.936
Total PCM mass fraction	0.785
Material properties	
ρ_h	2299 kg.m^{-3}
$c_{p,h}$	
solid	1540 J.kg.$^{-1}$.K^{-1}
liquid	1454 J.kg.$^{-1}$.K^{-1}
λ_{PCM}	
solid	0.720 W.m^{-1}.K^{-1}
liquid	0.515 W.m^{-1}.K^{-1}
$\lambda_{eq,s}$	
$R_{text} < r < R_{text}$ + 10 mm	6.92 W.m^{-1}.K^{-1}
R_{text} + 10 mm $< r < R_{text}$ + 30 mm	Variable (bounded values: 5.61 – 3.48 W.m^{-1}.K^{-1})
$r > R_{text}$ + 30 mm	0.720 W.m^{-1}.K^{-1}
Mesh properties	
Number of cells	
axial direction	10
radial direction	9
total	110

4.2 Results

The present computations deal with the same test cases as the ones presented in Section 3. In the current situation, the space steps are Δz = 54.0 mm and Δr = 1.85 mm. The HTF pressure is chosen so that the saturation temperature is equal to the desired wall temperature, and accordingly, the internal heat transfer coefficient is set to $\alpha_{tint} = 10^6$ W.m^{-2}.K^{-1}. Water vapor, with a slight superheating of 0.1°C, is injected at the top with a 0.05 kg.s^{-1} mass flow-rate.

The whole system is solved with an in-house code, in Scilab language. For Eqs. (19), (20), (25) and (27), a classic finite volume method is used. The temporal integration is fully implicit. The numerical resolution is done separately for the HTF on the one hand, and for the tube thickness and the homogeneous material on the other hand. For these two blocks, the convergence criterion is based on the variation of the solved quantities from one iteration to another. On the HTF side, convergence is reached when the relative variation of mass enthalpy and mass flow in each mesh cell is below 10^{-12}. For the second block, the total mass enthalpy is normalized by its initial value, and convergence is assumed to be reached when the variation of this normalized mass enthalpy is below 10^{-8}.

The main focus is very much on the ability to reproduce the storage behavior, that is to say to represent the variation of energy inside the module. Therefore, the temporal evolution of the energy accumulated by the PCM is represented on Figure 12 for the three cases, for both the CFD model and the reduced model. Overall, the agreement between the system model and the CFD results is good: the mean discrepancy between the two models is 4.8% for T_w = 328°C, 6.8% for T_w = 318°C, and 14% for T_w = 310°C. In the latter case, it is important to mention that this discrepancy probably comes from the intrinsic limit of the Nusselt correlation that fundamentally holds only for the liquid region. However, as can be seen in Figure 13, the mushy region is far more pronounced for the lower HTF temperature. As a consequence, the method is here less reliable.

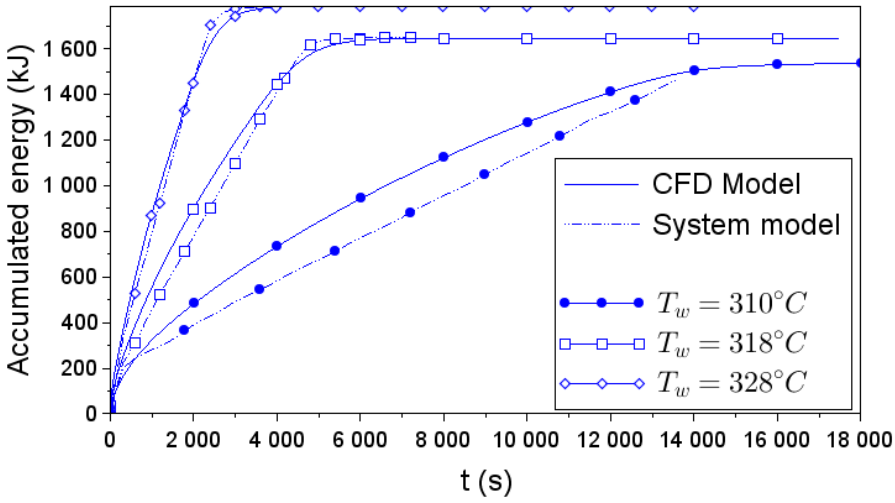
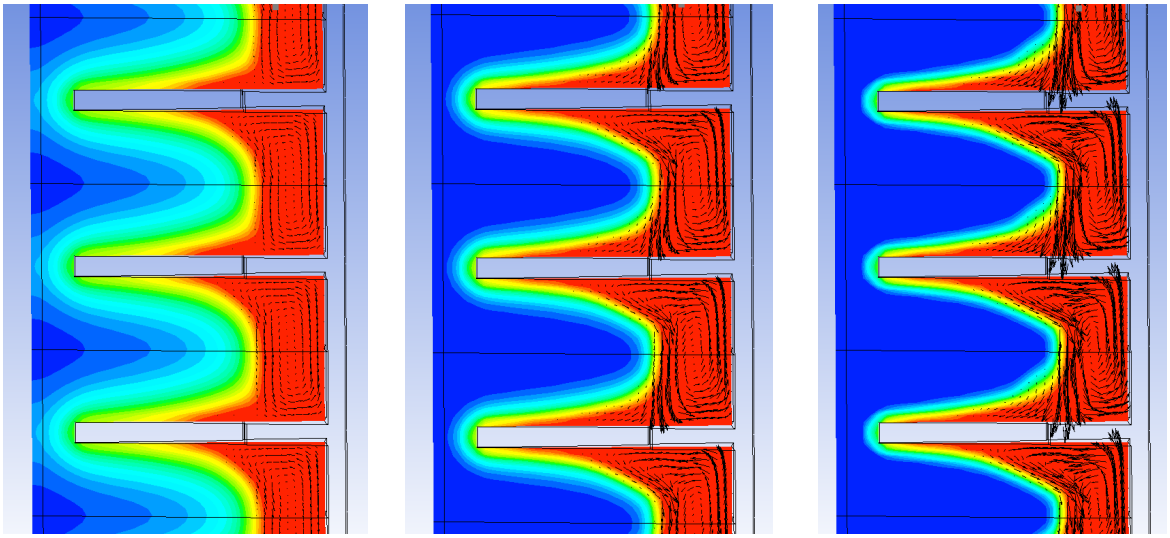


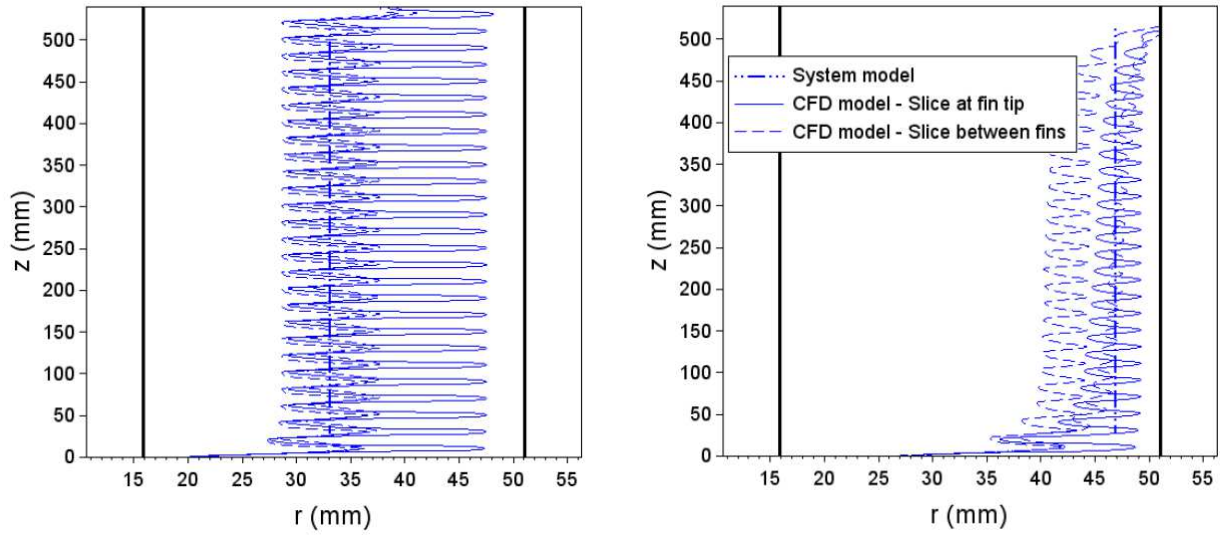
Figure 12: Comparisons of the energy accumulated in the PCM, the tube and the fins during melting at a constant and uniform wall temperature, for the CFD and system models



(a) T_w = 310°C (b) T_w = 318°C (c) T_w = 328°C

Figure 13: Liquid fraction and velocity fields in a vertical plane for the three CFD computations

Shapes of the phase front are presented in Figure 14 at two different instants for the case T_w = 328°C. Though the initial CFD results logically match the fins' shape, the mean front position predicted by the system model is in good agreement with these results. This evidences the capability of the reduced model to reproduce the melting rate.



(a) t = 900s (b) t = 1800s

Figure 14: Comparisons of the phase fronts predicted by the CFD and system models for T_w = 328°C (black lines represent the boundaries of the PCM domain. Left: outer tube wall. Right: external domain boundary.)

All in all, the overall agreement between the reduced model and the complete CFD model is relatively good, and these results are very promising. Finally, to further highlight the assets of the present method, comparisons of the computational times needed to obtain the results are presented in Table 3. It is straightforward to notice that a considerable reduction can be achieved, resulting in 10 to 40 times lower CPU costs.

Table 3: Computational times for the CFD model and the reduced system model

	T_w = 310°C	T_w = 318°C	T_w = 328°C
CFD model	289 h (≈12 days)	132 h (5.5 days)	158 h (≈ 7 days)
System model	29 h	8 h	4 h

5 Conclusion

A reduced model has been built to carry out fast and accurate simulations of a dual two-phase storage of steam, composed of a shell containing a PCM crossed by several finned tubes containing a liquid/vapor heat transfer fluid. The corresponding system is based on an effective thermal conductivity which is determined using a heat transfer correlation with specific non-dimensional numbers. This correlation mainly involves the Nusselt and Rayleigh numbers which are linked from previous simulations of the phase change material's behavior, obtained with fine 3D computational fluid dynamics calculations. A specific study was made to determine the best suited definitions for the characteristic length and the mean PCM temperature involved in the Nusselt and Rayleigh numbers. In summary, the present method proposes to avoid the usual tuning of endogenous parameters; instead, a Nusselt correlation is determined and then used directly in the system model without any other *a posteriori* calibration.

When comparing the results of the two approaches, the agreement obtained is rather good for the three test cases considered (three different temperatures of the inner tube wall T_w = 310, 318 and 328°C with the PCM initially solid at 290°C). The evolution of the accumulated energy over time is predicted by the system model with an average deviation of 4 to 14% from the CFD results. The time required for the simulation of a melting is 10 to 40 times less for the reduced model than for the CFD model.

Thus, the current method appears to be very promising, making it possible to consider future easy and fast designs of latent heat storage systems, and/or multiple sensitivity analysis that would be too prohibitive otherwise. In the near future, it is planned to consolidate first the determination of the Nusselt correlation. Then, the reduced model will be further developed to remove its basic assumptions, that can easily be avoided; at the same time, it will be validated on numerous test cases in order to bound its precision, together with the savings in computational cost.

Last but not least, an important prospect will be the development of a similar multi-scale methodology for steam discharge, involving PCM solidification, and boiling of the heat transfer fluid. During solidification in a PCM heat storage module, the heat transfers are generally mainly conductive. The reduced model will have to be adapted.

References

[1] "Technology Roadmap - Solar Thermal Electricity," IEA, 2014.

[2] M. Medrano, A. Gil, I. Martorell, X. Potau, and L. F. Cabeza, "State of the art on high-temperature thermal energy storage for power generation. Part 2—Case studies," *Renewable and Sustainable Energy Reviews*, vol. 14, no. 1, pp. 56–72, Jan. 2010.

[3] A. Fernández-García, E. Zarza, L. Valenzuela, and M. Pérez, "Parabolic-trough solar collectors and their applications," *Renewable and Sustainable Energy Reviews*, vol. 14, no. 7, pp. 1695–1721, Sep. 2010.

[4] J. Birnbaum, T. Hirsch, M. Eck, R. Pitz-Paal, M. Fichtner, and G. Zimmermann, "A concept for future parabolic trough based solar thermal power plants," in *15th International Conference on the Properties of Water and Steam, Berlin, Germany*, 2008.

[5] W.-D. Steinmann and M. Eck, "Buffer storage for direct steam generation," *Solar Energy*, vol. 80, no. 10, pp. 1277–1282, Oct. 2006.

[6] D. Laing, C. Bahl, T. Bauer, D. Lehmann, and W.-D. Steinmann, "Thermal energy storage for direct steam generation," *Solar Energy*, vol. 85, no. 4, pp. 627–633, Apr. 2011.

[7] X. Ju, C. Xu, X. Li, X. Du, and Y. Yang, "Numerical analysis of thermal storage performance with high-temperature phase change materials operated by condensing steam," *Solar Energy*, vol. 117, pp. 213–223, Jul. 2015.

[8] P. Garcia, V. Vuillerme, M. Olcese, and N. El Mourchid, "Design and modelling of an innovative three-stage thermal storage system for direct steam generation CSP plants," *AIP Conference Proceedings*, vol. 1734, p. 050015, 2016.

[9] A. Caron-Soupart, J.-F. Fourmigué, P. Marty, and R. Couturier, "Performance analysis of thermal energy storage systems using phase change material," *Applied Thermal Engineering*, vol. 98, pp. 1286–1296, Apr. 2016.

[10] M. Martinelli, F. Bentivoglio, A. Caron-Soupart, R. Couturier, J.-F. Fourmigue, and P. Marty, "Experimental study of a phase change thermal energy storage with copper foam," *Applied Thermal Engineering*, vol. 101, pp. 247–261, May 2016.

[11] K. S. do Couto Aktay, R. Tamme, and H. Müller-Steinhagen, "Thermal Conductivity of High-Temperature Multicomponent Materials with Phase Change," *Int J Thermophys*, vol. 29, no. 2, pp. 678–692, Apr. 2008.

[12] P. Garcia, M. Olcese, and S. Rougé, "Experimental and Numerical Investigation of a Pilot Scale Latent Heat Thermal Energy Storage for CSP Power Plant," *Energy Procedia*, vol. 69, pp. 842–849, May 2015.

[13] S. Tiari, S. Qiu, and M. Mahdavi, "Numerical study of finned heat pipe-assisted thermal energy storage system with high temperature phase change material," *Energy Conversion and Management*, vol. 89, pp. 833–842, Jan. 2015.

[14] F. Fornarelli *et al.*, "CFD analysis of melting process in a shell-and-tube latent heat storage for concentrated solar power plants," *Applied Energy*, vol. 164, pp. 711–722, Feb. 2016.

[15] S. S. Mostafavi Tehrani, G. Diarce, and R. A. Taylor, "The error of neglecting natural convection in high temperature vertical shell-and-tube latent heat thermal energy storage systems," *Solar Energy*, vol. 174, pp. 489–501, Nov. 2018.

[16] M. Lacroix, "Numerical simulation of a shell-and-tube latent heat thermal energy storage unit," *Solar Energy*, vol. 50, no. 4, pp. 357–367, Apr. 1993.

[17] H. A. Adine and H. El Qarnia, "Numerical analysis of the thermal behaviour of a shell-and-tube heat storage unit using phase change materials," *Applied Mathematical Modelling*, vol. 33, no. 4, pp. 2132–2144, Apr. 2009.

[18] R. Waser *et al.*, "Fast and experimentally validated model of a latent thermal energy storage device for system level simulations," *Applied Energy*, vol. 231, pp. 116–126, Dec. 2018.

[19] H. A. Zondag, R. de Boer, S. F. Smeding, and J. van der Kamp, "Performance analysis of industrial PCM heat storage lab prototype," *Journal of Energy Storage*, vol. 18, pp. 402–413, Aug. 2018.

[20] M. Johnson, J. Vogel, M. Hempel, B. Hachmann, and A. Dengel, "Design of high temperature thermal energy storage for high power levels," *Sustainable Cities and Society*, vol. 35, no. Supplement C, pp. 758–763, Nov. 2017.

[21] S. S. Mostafavi Tehrani, Y. Shoraka, G. Diarce, and R. A. Taylor, "An improved, generalized effective thermal conductivity method for rapid design of high temperature shell-and-tube latent heat thermal energy storage systems," *Renewable Energy*, vol. 132, pp. 694–708, Mar. 2019.

[22] J. L. Wright, "A Correlation to Quantify Convective Heat Transfer Between Vertical Window Glazings," *ASHRAE Transactions*, vol. 102, Part 1, pp. 940–946, 1996.

[23] S. W. Churchill and H. H. S. Chu, “Correlating equations for laminar and turbulent free convection from a vertical plate,” *International Journal of Heat and Mass Transfer*, vol. 18, no. 11, pp. 1323–1329, Nov. 1975.
[24] T. Hirata and K. Nishida, “An analysis of heat transfer using equivalent thermal conductivity of liquid phase during melting inside an isothermally heated horizontal cylinder,” *International Journal of Heat and Mass Transfer*, vol. 32, no. 9, pp. 1663–1670, Sep. 1989.
[25] W.-W. Wang, L.-B. Wang, and Y.-L. He, “The energy efficiency ratio of heat storage in one shell-and-one tube phase change thermal energy storage unit,” *Applied Energy*, vol. 138, pp. 169–182, Jan. 2015.
[26] K. Yang, N. Zhu, C. Chang, H. Yu, and S. Yang, “Numerical analysis of phase-change material melting in triplex tube heat exchanger,” *Renewable Energy*, vol. 145, pp. 867–877, Jan. 2020.
[27] C. Beust, E. Franquet, J.-P. Bédécarrats, P. Garcia, and J. Pouvreau, “Influence of the Modeling Parameters on the Numerical CFD Simulation of a Shell-and-Tube Latent Heat Storage System with Circular Fins,” presented at the SolarPACES 2018, Casablanca, Morocco, 2018, p. 8.
[28] D. Bestion and C. Morel, “Balance equations,” in *Thermal-Hydraulics of Water Cooled Nuclear Reactors*, Elsevier, 2017, pp. 167–244.
[29] V. R. Voller, C. R. Swaminathan, and B. G. Thomas, “Fixed grid techniques for phase change problems: A review,” *Int. J. Numer. Meth. Engng.*, vol. 30, no. 4, pp. 875–898, Sep. 1990.
[30] V. R. Voller and C. Prakash, “A fixed grid numerical modelling methodology for convection-diffusion mushy region phase-change problems,” *International Journal of Heat and Mass Transfer*, vol. 30, no. 8, pp. 1709–1719, Aug. 1987.
[31] A. Lomonaco, D. Haillot, E. Pernot, E. Franquet, and J.-P. Bédécarrats, “Sodium nitrate thermal behavior in latent heat thermal energy storage: A study of the impact of sodium nitrite on melting temperature and enthalpy,” *Solar Energy Materials and Solar Cells*, vol. 149, pp. 81–87, May 2016.
[32] V. M. B. Nunes, C. S. Queirós, M. J. V. Lourenço, F. J. V. Santos, and C. A. Nieto de Castro, “Molten salts as engineering fluids – A review: Part I. Molten alkali nitrates,” *Applied Energy*, vol. 183, pp. 603–611, Dec. 2016.
[33] S. Kandlikar, M. Shoji, and V. K. Dhir, “Handbook of phase change: Boiling and condensation”, Taylor & Francis, 1999, ISBN 1-56032-634-4

[99] D. Laing, T. Bauer, N. Breidenbach, B. Hachmann, and M. Johnson. Development of high temperature phase-change-material storages. Applied Energy, 109:497 – 504, 2013.

[98] A. A. Al-Abidi, S. Mat, K. Sopian, M. Sulaiman, and A. T. Mohammad. Experimental study of melting and solidification of PCM in a triplex tube heat exchanger with fins. Energy and Buildings, 68, Part A:33 – 41, 2014.

[97] T. Pirasaci and D. Y. Goswami. Influence of design on performance of a latent heat storage system for a direct steam generation power plant. Applied Energy, 162:644 – 652, 2016

[96] C. Zauner, F. Hengstberger, M. Etzel, D. Lager, R. Hofmann, and H. Walter. Experimental characteri- zation and simulation of a fin-tube latent heat storage using high density polyethylene as PCM. Applied Energy, 179:237 – 246, 2016

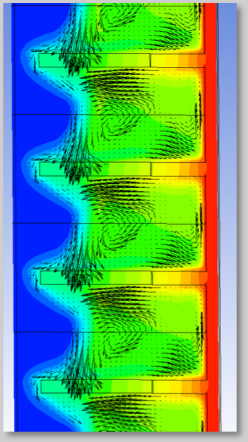
[95] M. Olcese, R. Couturier, JF. Fourmigue, P. Garcia, O. Raccurt, JF. Robin, B. Senechal, S. Rougé, B. Thonon, Design methodology and experimental platform for the validation of PCM storage modules for DSG solar plants. Energy Procedia 49 (2014) 945 – 955

[94] C. Beust, E. Franquet, J.-P. Bédécarrats, P. Garcia. A numerical investigation of some key factors for the simulation of convection-dominated melting. International Journal of Thermal Sciences. In revision.

[93] C. Beust. Modélisation multi-échelles d’un système de stockage thermique de vapeur par Matériau à Changement de Phase (MCP). PhD Thesis, Université de Pau et des Pays de l’Adour (in french). http://www.theses.fr/2019PAUU3029/document

[92] R. Bayón, E. Rojas, L. Valenzuela, E. Zarza, and J. León, “Analysis of the experimental behaviour of a 100 kWth latent heat storage system for direct steam generation in solar thermal power plants,” Applied Thermal Engineering, vol. 30, no. 17–18, pp. 2643–2651, Dec. 2010

[91] ANSYS Fluent. Theory Guide, Release 17.2, 2016



PCM

Fusion / solidification

$Nu(t,z) = f\big(Ra(t,z)\big)$

$\dot{m}_{HTF}$

Liquid PCM
+ fins / inserts

$\lambda_{eq} = f(t,z)$

Tube wall

Solid PCM +
fins / inserts

Water / steam

z

r

CFD Model

System Model